J Mater Sci: Mater Electron

Complex electrical impedance and modulus characterizations of ZnO:Sn thin films in a wide temperature range

Irmak Karaduman Er[1,*], Ali Orkun Çağırtekin[2], Ahmad Ajjaq[2], Memet Ali Yıldırım[3], Aytunç Ateş[4], and Selim Acar[2]

[1] Department of Medical Services and Techniques, Eldivan Medical Services Vocational School, Çankırı Karatekin University, Çankırı 18700, Turkey
[2] Department of Physics, Faculty of Science, Gazi University, Ankara 06560, Turkey
[3] Department of Electric and Electronic Engineering, Engineering Faculty, Erzincan Binali Yıldırım University, Erzincan 24100, Turkey
[4] Department of Metallurgy and Material Engineering, Engineering and Natural Sciences Faculty, Ankara Yıldırım Beyazıt University, Ankara 06010, Turkey

Received: 8 March 2021
Accepted: 6 April 2021

© The Author(s), under exclusive licence to Springer Science+Business Media, LLC, part of Springer Nature 2021

ABSTRACT

In this study, pure zinc oxide (ZnO) and tin-doped zinc oxide ($Zn_{1-x}Sn_xO$) thin films were synthesized using successive ionic layer adsorption and reaction (SILAR) method in 40 cycles with doping ratios x = 0.05, 0.10, 0.15, and 0.20. Subsequently, structural, optical, and electrical characteristics of all synthesized thin films were properly investigated by the appropriate techniques. For structural characterizations, X-ray diffraction (XRD) technique was employed, and the data demonstrated the appropriate hexagonal wurtzite structure of the synthesized thin films and predicted the decrease of crystallite size with Sn doping. Likewise, optical characterizations were carried out through ultraviolet–visible (UV–Vis) technique, and the data showed good transparency of ZnO thin film and confirmed the increase in transparency and bandgap upon Sn doping. Additionally, to probe the electrical aspects of the synthesized thin films, impedance, modulus, and conductivity analyses were carried out as a function of frequency in a wide temperature range (450–750 K). The results demonstrated the critical effect of temperature and Sn doping ratio in ZnO thin films. At high enough temperatures, inductive effects became evident in the low-frequency region of all the thin films. And at all temperatures, 5 wt%- and 10 wt%-doped films exhibited extreme responses in the investigated doping range, where the former and the latter showed, respectively, highest and lowest conductivity as well as lowest and highest possibility of grain effects in the film structure. This behavior was confirmed using two different analysis techniques with two separate data sets, (Z, θ) and (C, G).

Address correspondence to E-mail: irmakkaradumaner@karatekin.edu.tr

https://doi.org/10.1007/s10854-021-05935-1
Published online: 24 April 2021

1 Introduction

Metal oxide semiconductor (MOS) materials, particularly transparent conducting oxide (TCO) materials, are recently part and parcel of many domains in nanotechnology due to their distinctive features. Indeed, TCO thin films are electrically conductive and optically transparent and hence are widely used in disciplines like electronics and optoelectronics.

As a good candidate of TCO materials, zinc oxide (ZnO) is widely researched due to its practical and low-cost preparation, good conductivity and transparency, broad bandgap, strong stability, and the abundance of Zn in nature [1]. By virtue of these characteristics and plenty others, ZnO was favored to be used in various industrial and technological implementations as follows: energy-saving and heat-protecting optical windows in solar cells [2], transducers [3], transistors [4], transparent electrodes in liquid–crystal displays (LCDs) [5], organic light emitting diodes (OLEDs) [5], and gas sensors [6]. By convention, ZnO is an n-type semiconductor due to non-stoichiometric intrinsic defects, like zinc interstitials (I_{Zn}) and oxygen vacancies (V_O), though it was recently proved that V_O's are the superior reason of the n-type conductivity [7]. *n*-ZnO has a comparatively broad direct bandgap of about 3.37 eV at room temperature.

Doping is one efficient way to tune several characteristics by mutating the surface morphology and altering the conduction and relaxation mechanisms of charge carriers in the material. For several reasons, tin (Sn) is one good choice to dope ZnO thin films. Zinc ($_{30}$Zn: [Ar] $3d^{10}$ $4s^2$) and tin ($_{50}$Sn: [Kr] $4d^{10}$ $5s^2$ $5p^2$) atoms have, respectively, two and four valence electrons in their outer shells. This tells that doping with Sn would enrich the conduction band of ZnO with more free electrons. Moreover, in a tetrahedral coordination type, Zn^{2+} and Sn^{4+} ions have relatively close radius values of 74 pm and 71 pm, respectively [8]. This suggests that doping with Sn would allow a smooth exchange of ions without causing any serious deformation in the host ZnO lattice.

The ultimate goal of this work is to probe the possible impacts of Sn doping on the structural, optical, and electrical properties of ZnO thin films produced using successive ionic layer adsorption and reaction (SILAR) method by varying Sn percent concentration in ZnO:Sn thin film as 5%, 10%, 15%, and 20%. Priority was often given to SILAR because it can be performed at room temperature and does not require high-pressure or special substrate conditions, which makes it a low-cost and practical synthesis technique. The structural and optical analyses were performed using XRD and UV–Vis techniques, respectively. Moreover, the electrical analysis was carried out using impedance, modulus, and conductivity spectra in a wide temperature range to investigate the different resistive, capacitive, and inductive effects in the films' structures and to estimate the individual contributions of different elements (grains, grain boundaries and electrodes) in the sample to the collective electrical behavior adopted by the thin film.

2 Experiment

In this study, SILAR method was chosen for the synthesis of pure ZnO and $Zn_{1-x}Sn_xO$ (x = 0.05, 0.10, 0.15, 0.20) thin films. In this process, glass substrates (8×25 mm^2) were used, over which the interdigitated (IDE) gold electrodes were evaporated. Then, the thin films were synthesized over the IDE gold-coated glass substrates using SILAR method. To synthesize the thin films, aqueous zinc-ammonia complex ions ($[Zn(NH_3)_4]^{2+}$) and aqueous tin-ammonia complex ions ($[Sn(NH_3)_4]^{4+}$) were selected as cation precursors, in which trace metal basis of $ZnCl_2$ (99.9%, Sigma-Aldrich) of 0.1 M and $SnCl_4$ (99.9%, Sigma-Aldrich) of 0.1 M were used as respective sources of Zn and Sn, along with aqueous ammonia solution (NH_3—28%, Sigma-Aldrich). Deionized water was used as a solvent. The obtained complexes were mixed in appropriate ratios according to the composition of ZnO, $Zn_{0.95}Sn_{0.05}O$, $Zn_{0.90}Sn_{0.10}O$, $Zn_{0.85}Sn_{0.15}O$, and $Zn_{0.80}Sn_{0.20}O$ thin films.

First of all, the glass substrates with IDE gold contacts were individually cleaned through multiple steps. After cleaning, solutions were prepared with different Sn doping ratios. A SILAR cycle consists of four consecutive stages, each of which has a specific duration: dipping the substrates in the prepared solutions, immersing them in hot water, holding them in air environment, and then immersing them in pure water at room temperature. These steps complete one SILAR cycle, and more details on SILAR were already reported in our previous work [9]. All the thin films in this study were synthesized in 40 SILAR cycles without any annealing.

The crystallinity of the synthesized thin films was characterized by X-ray diffraction (XRD, Rigaku Ultima-IV X-ray diffractometer) using Cu-Kα radiation source with λ = 1.5405 Å in 20° to 70° 2θ range. To study the optical properties of the thin films, absorption and transmission measurements were carried out using a Perkin-Elmer UV–Vis Lambda 2S Spectrometer with a wavelength resolution higher than ±0.3 nm at room temperature. Electrical characterizations were performed through two distinct experimental data sets—(Z, θ) and (C, G)—using the impedance analyzer measurement system which consists of a Keysight E4990A impedance analyzer, LakeShore 325 temperature controller, test cell, and computer system. The C–V measurements were performed by using Keysight E4990A impedance analyzer in 1 kHz to 1.5 MHz frequency range, and the temperature-dependent measurements were carried out from 450 to 750 K in 25 K steps. The data were gathered in real time using a computer with the relevant data collection hardware and software.

3 Results and discussion

3.1 Structural characterization

Prior to analyzing the optical and electrical characteristics of the synthesized films, investigating their structural characteristics is a crucial step. For this aim, XRD technique was utilized and the obtained XRD patterns of all the synthesized thin films are given in Fig. 1.

It is observed that the dominant crystal phase in all the XRD patterns of the thin films is the hexagonal wurtzite phase of ZnO (JCPDS card no. 36-1451). Also, the characteristic peaks belonging to the tetragonal phase of SnO_2 thin film (JCPDS card no. 41-1445) began to appear and the peak positions shifted to larger diffraction angles with the increase in Sn concentration. This can be associated to the change of unit cell size due to the differences of the ionic radii of Zn^{2+} (74 pm) and Sn^{4+} (71 pm). Same behavior was also reported earlier in the literature by Andolsi et. al. in a study on Sn-doped ZnO [1]. Changes to diffraction peaks may also reflect some changes in crystal parameters. The XRD parameters of thin films are given in Table 1.

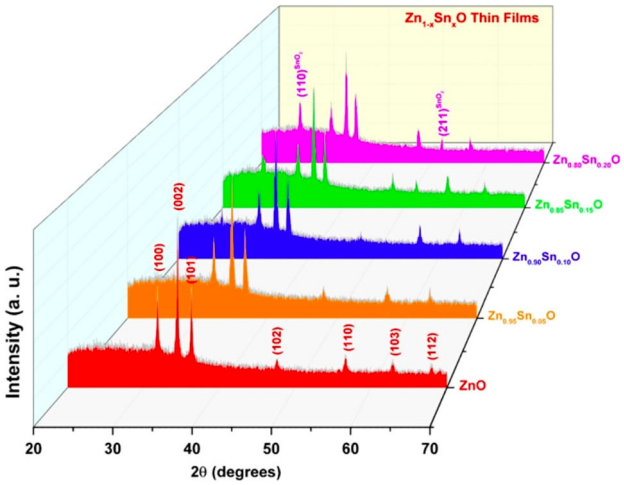


Fig. 1 XRD patterns of all synthesized thin films at room temperature

The lattice parameters (a and c) were calculated using Eq. (1) [10], and the obtained a and c values are compatible with the literature [11].

$$\frac{1}{d_{hkl}^2} = \frac{4}{3}\left(\frac{h^2 + hk + k^2}{a^2}\right) + \frac{l^2}{c^2}. \quad (1)$$

The unit cell volume (V) was calculated using Eq. (2) [12],

$$V = \frac{\sqrt{3}}{4}a^2c. \quad (2)$$

The mean crystallite size (D) was estimated according to the broadening of the highest intensity peak corresponding to the (002) diffraction plane using the Debye–Scherrer formula given in Eq. (3) [13],

$$D = \frac{K\lambda}{\beta\cos\theta}, \quad (3)$$

where K is a shape factor (K = 0.9 was used in Eq. (3) and the calculated values of D should be considered as estimates only, because K depends on the crystallite geometry and size distribution. Even small variations in the K values can generate large variations in D), λ is the wavelength of X-ray, and β is the full width at half maximum (FWHM) value. It is clearly seen that the estimated average crystallite size of pure ZnO decreased significantly with the first Sn doping, and then continued to decrease slightly with the further increase in Sn doping percentage.

The morphological characterization by scanning electron microscopy (SEM) as well as elemental

Table 1 XRD parameters of all synthesized thin films

	(*hkl*)	2θ(°)	β	D(nm)	a(Å)	c(Å)	c/a	$V\left(\text{Å}^3\right)$
ZnO	(100)	31.863	0.286	65	3.240	5.195	1.604	23.608
	(002)	34.497	0.248					
	(101)	36.340	0.266					
$Zn_{0.95}Sn_{0.05}O$	(100)	32.354	0.344	43	3.192	5.130	1.607	22.631
	(002)	34.943	0.368					
	(101)	36.832	0.399					
$Zn_{0.90}Sn_{0.10}O$	(110)	27.859	0.177	43	3.187	5.123	1.607	22.536
	(100)	32.408	0.397					
	(002)	34.994	0.380					
	(101)	36.883	0.410					
$Zn_{0.85}Sn_{0.15}O$	(110)	26.519	0.170	42	3.184	5.119	1.607	22.476
	(100)	32.434	0.178					
	(002)	35.029	0.404					
	(101)	36.886	0.367					
$Zn_{0.80}Sn_{0.20}O$	(110)	26.829	0.418	41	3.195	5.123	1.604	22.640
	(100)	32.337	0.479					
	(002)	34.999	0.391					
	(101)	36.697	0.426					

characterization by energy-dispersive X-ray spectroscopy (EDXS) of all synthesized thin films are published in Fig. 3 in our previous work [9]. By EDXS, the stoichiometric increase in Sn atomic percentage in the actual composition confirmed the trend of doping during SILAR chemical synthesis.

3.2 Optical characterization

By UV–Vis technique, the optical transmission spectra of pure and Sn-doped ZnO thin films are offered in Fig. 2a. All the thin films had a sharp increase in transmittance at about 350 nm. Pure ZnO thin film showed a transmittance of about 60% in the visible range which confirms its good transparency as a TCO material. Besides, with Sn doping, transmission increased up to about 85% in the visible range.

As is shown by the inset of Fig. 2a, the optical direct bandgaps were evaluated by extrapolation of the linear region of $(\alpha h\nu)^2$ versus $(h\nu)$ plots to $(\alpha h\nu)^2 = 0$ using Tauc relation [1],

$$\alpha h\nu = A\left(h\nu - E_g\right)^n, \tag{4}$$

where A is a constant, $h\nu$ is incident photon energy, E_g is optical bandgap, α is linear absorption coefficient, and in this study $n = 1/2$ due to the linearity of the tails at the band edges which corresponds to direct band transitions. The bandgap values are found as follows: 3.16 eV, 3.18 eV, 3.21 eV, 3.23 eV, and 3.27 eV for ZnO, $Zn_{0.95}Sn_{0.05}O$, $Zn_{0.90}Sn_{0.10}O$, $Zn_{0.85}Sn_{0.15}O$, and $Zn_{0.80}Sn_{0.20}O$ thin films, respectively. Clearly, the bandgap increased with the increase in Sn doping ratio, and this is equivalent to the shift in the optical transmission spectra towards lower wavelength (Hypsochromic shift or blue shift). Similar behavior was observed by Andolsi et al. in a study on Sn-doped ZnO thin films [1]. The gradual increase in bandgaps with Sn doping can be attributed to the formation of new localized states with higher emission energy in the film structure and is mainly due to the Burstein-Moss effect [14]. Fundamentally, electrons from donor atoms fill up the states near the minimum of the conduction band and thus effectively lift the bandgap up. Moreover, XRD data showed that the mean crystallite size decreases with Sn doping. A decrease in crystallite size leads to a decrease in the number of overlapping energy levels and thus provokes a shrinkage of the bands and an increase in the bandgap.

In addition, bowing parameter is significant for investigating the energy bandgap of ternary compound semiconductors. It can be determined by a parabolic fit of the plot of bandgap versus doping concentration in the ternary compounds as is shown in Fig. 2b. The energy bandgap of ternary compound semiconductor such as $Zn_{1-x}Sn_xO$ can be described by fitting the energy bandgap values to a quadratic equation of the form,

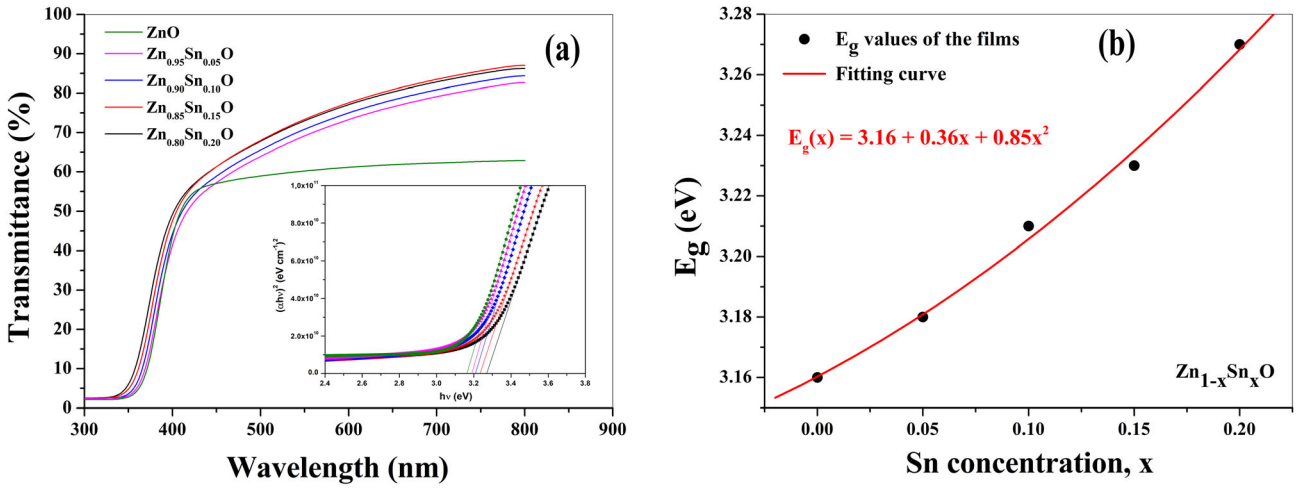


Fig. 2 **a** Optical transmission spectra and (inset) $(\alpha h\nu)^2$ versus $(h\nu)$ plots, and **b** E_g versus x plot and fitting curve to a suitable parabola of $Zn_{1-x}Sn_xO$ (x = 0.05, 0.10, 0.15, 0.20) thin films

$$E_g(x) = (1-x)E(0) + xE(1) - bx(1-x), \quad (5)$$

where x is the doping ratio of Sn and b is the bowing parameter. A polynomial fitting of the present bandgap data to parabola, as in Eq. (5), gives,

$$E_g(x) = 3.16 + 0.36x + 0.85x^2, \quad (6)$$

with a bowing parameter $b = 0.85$ eV. These results demonstrate that $Zn_{1-x}Sn_xO$ thin films form an alloy that fits the outcomes of XRD analysis. This value is slightly higher than that published by Yıldırım et al. of 0.76 eV in highly doped $Zn_{2(1-x)}Sn_xO_2$ heterostructures [14].

3.3 Electrical characterization

All the investigated thin films adopted similar electrical behavior as a function of frequency and temperature, but with different numerical values. And so, throughout this section, only the films that showed the extreme responses with Sn doping ($Zn_{0.95}Sn_{0.05}O$ and $Zn_{0.90}Sn_{0.10}O$) were offered, along with the pure ZnO thin film as reference. However, all results from all the films were superimposed for comparison where necessary.

3.3.1 *Impedance study*

Impedance spectroscopy is a powerful tool that has been widely used to analyze electrical properties arising from dielectric relaxation and conduction mechanisms at nanoscale. At nanoscale, materials can be thought of as an assembly of grains, grain boundaries, and grain-electrode interfaces, each of which can influence the overall electrical behavior adopted by the material. This influence can be understood by utilizing complex impedance spectroscopy method [15]. Generally, the complex electrical impedance can be written in the form,

$$Z^* = Z' + iZ'', \quad (7)$$

where $Z' = Z\cos\theta$ and $Z'' = Z\sin\theta$ are, respectively, the corresponding real and imaginary components of the complex impedance, Z is the measured impedance magnitude, and θ is the measured I-V phase difference. Through impedance analysis, two different types of plots can be analyzed: Bode plots of Z' and Z'' versus frequency and Nyquist plot of Z'' versus Z'.

Figure 3 shows the frequency dependence of Z' of the films at various temperatures. Obviously, Z' decreased as frequency increased. In fact, in the low-frequency region, two separate behaviors were spotted at two different temperature ranges. At low temperatures, Z' decreased steeply, while at high temperatures (475 K and beyond), Z' remained initially constant and then decreased flatly with the further increase in frequency. And at high enough frequencies (around 0.1MHz and beyond), all Z' plots exhibited the same asymptotic behavior and became independent of frequency and temperature which can be due to the dominance of space charge polarizations at high energies [16]. Moreover, all films exhibited negative temperature coefficient of resistance (NTCR) and showed to a great extent a typical

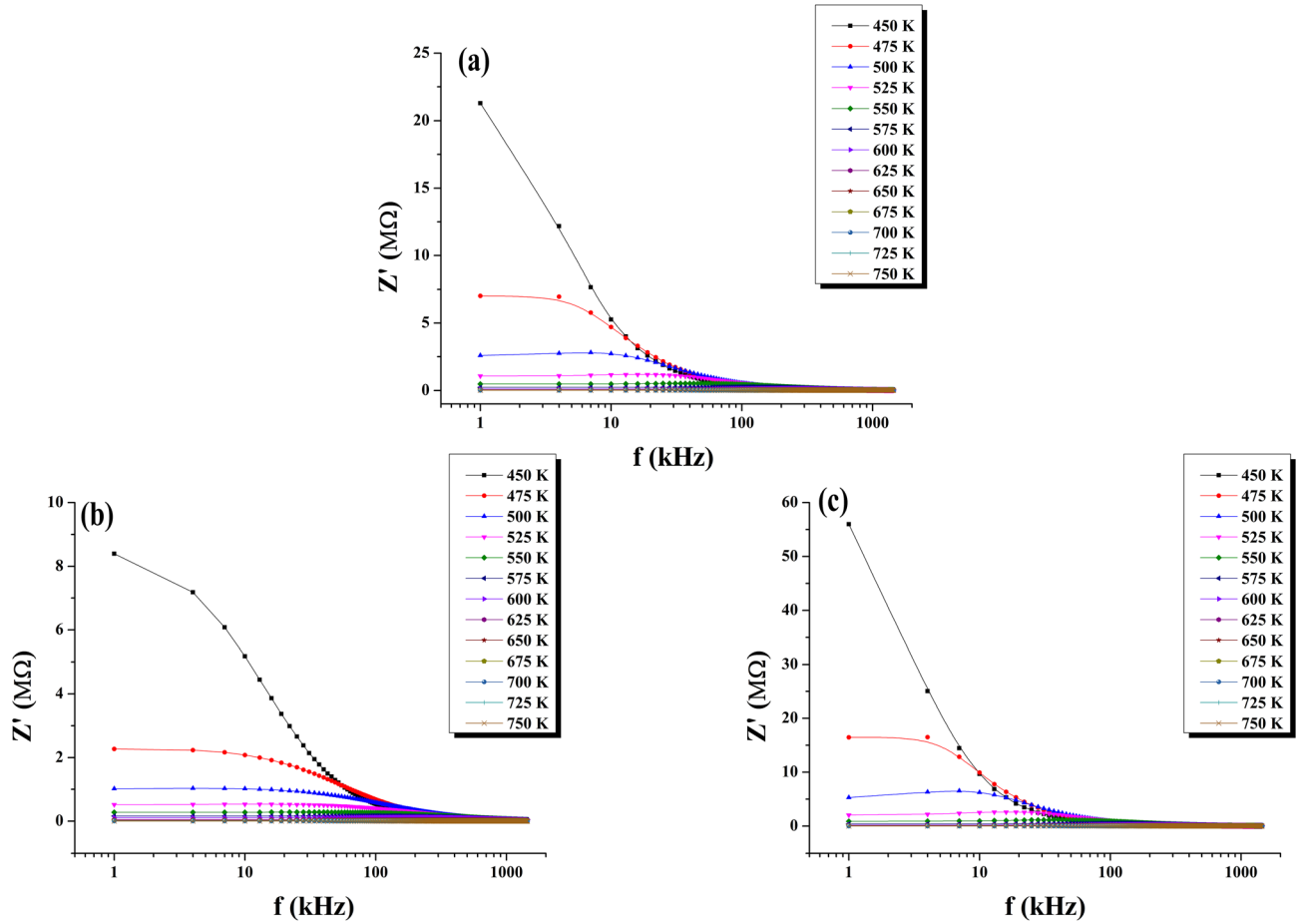


Fig. 3 Frequency response of Z' at different temperatures for **a** pure ZnO, **b** $Zn_{0.95}Sn_{0.05}O$, and **c** $Zn_{0.90}Sn_{0.10}O$ thin films

semiconductor behavior. Besides that, in comparison with pure ZnO thin film, it is clearly seen that Z' values are much smaller in the 5 wt%-doped ZnO and much larger in the 10 wt.%-doped ZnO at all temperatures.

Figure 4 shows the frequency dependence of Z'' of the films at various temperatures. In the investigated temperature range, two different behaviors at two separate temperature ranges were detected. At low temperatures (450–575 K), with increasing frequency, Z'' values initially increased and then decreased leaving a peak that decreased and shifted to high frequencies with the relative increase in temperature. A shift to higher frequencies implies a shift to lower relaxation times due to the accelerated hopping rate of charge carriers. At high temperatures (600–750 K), another minor relaxation peak started to appear in the low-frequency region, but it was negligible in the 5 wt%-doped ZnO thin film. Both low-frequency and high-frequency peaks decreased and shifted to higher frequency as temperature increased and the latter disappeared entirely at high temperatures. Also, similar to Z' plots, at high frequencies (0.1MHz and beyond), all Z'' curves tend to merge and become almost independent of both frequency and temperature which can be attributed also to the aggregation of space charge polarizations.

Figure 5 shows Z'' versus Z' Nyquist plots of the films at various temperatures. Obviously, all films revealed common behavior as a function of temperature. Compatible to Bode plots of Z'' in Fig. 4, at low temperatures, especially from $T = 450$ K and beyond, one semicircular relaxation arc with negative capacitive reactance (X_C) was spotted, and all semicircles decreased in radius with the further increase in temperature. This demonstrates a decrease in the film resistivity with the increase in temperature. At high temperatures, especially from $T = 600$ K and beyond, a clear spiral pattern at low frequency was detected in Nyquist plots of all the thin films, but it was very

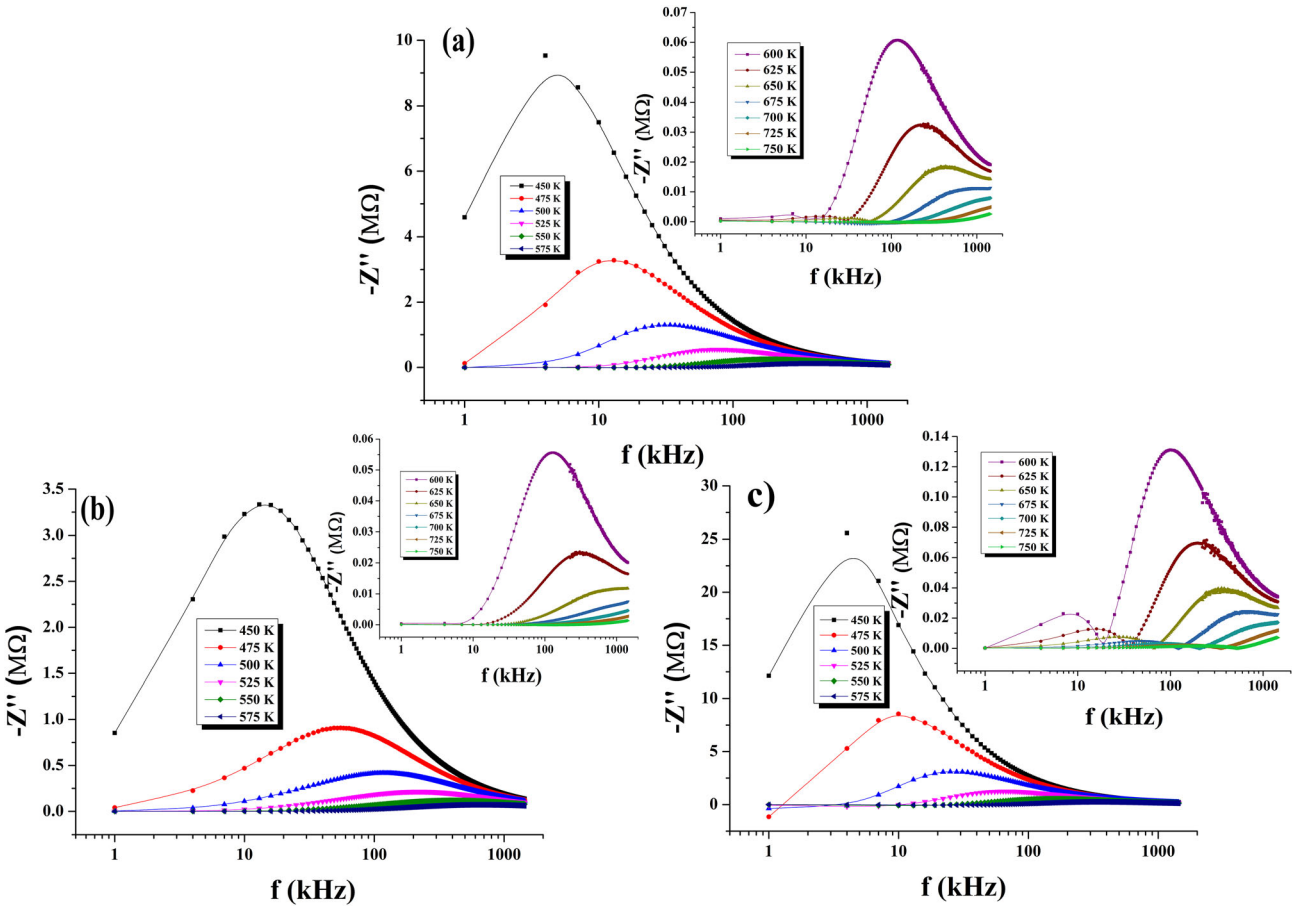


Fig. 4 Frequency response of Z'' at different temperatures for **a** pure ZnO, **b** $Zn_{0.95}Sn_{0.05}O$, and **c** $Zn_{0.90}Sn_{0.10}O$ thin films

negligible for 5 wt%-doped films. Such a spiral pattern can be an evidence to the presence of two frequency-dependent elements in the films' structures: X_C at high frequencies and positive inductive reactance (X_L) at low frequencies. The spiral semicircle formed at high temperatures can be directly related to the second peak seen in Bode plots of Z'' and is, in this case, due to inductive effects in the films' structures and this was confirmed by fit analysis in the next part. The appearance of this inductive behavior at low frequencies can be mostly associated with the non-linearity of time-dependence of conductance induced by voltage change [17].

Equivalent circuit modeling is a practical method to figure out the contribution of nanostructures in a sample to the overall collective behavior. Often, different nanostructure components are represented by four main passive circuit elements: resistors, capacitors, inductors, and constant phase elements (CPEs).

The experimental data of all the thin films at $T =$ 550 K and 600 K was best fitted to R(CR)(QR)(CR) and R(QR(LR)) circuit models, respectively. Fitting plots are shown in Fig. 6, where the inset figure displays the equivalent electrical circuit of the used model. The estimated values of the fit parameters are given in Table 2. At both temperatures, the CPE effect (represented by Q) is present. There are different factors that cause a CPE. CPE gives a measure of the modification of interfacial impedance by some exponent $\alpha(0 \leq \alpha \leq 1)$, known as the frequency power of the relevant relaxation mode which is a measure of the deviation from Debye relaxation mode. The CPE effect that appeared in the films can be best attributed to electrode roughness [18] due to which electrodes do not behave as a pure capacitance, but rather as an impedance displaying a frequency-dependent phase angle less than 90° (specifically $90° \times \alpha$), and it was calculated using the formula [19],

$$Z_{CPE} = \frac{Q}{(i\omega)^{\alpha}}, \tag{8}$$

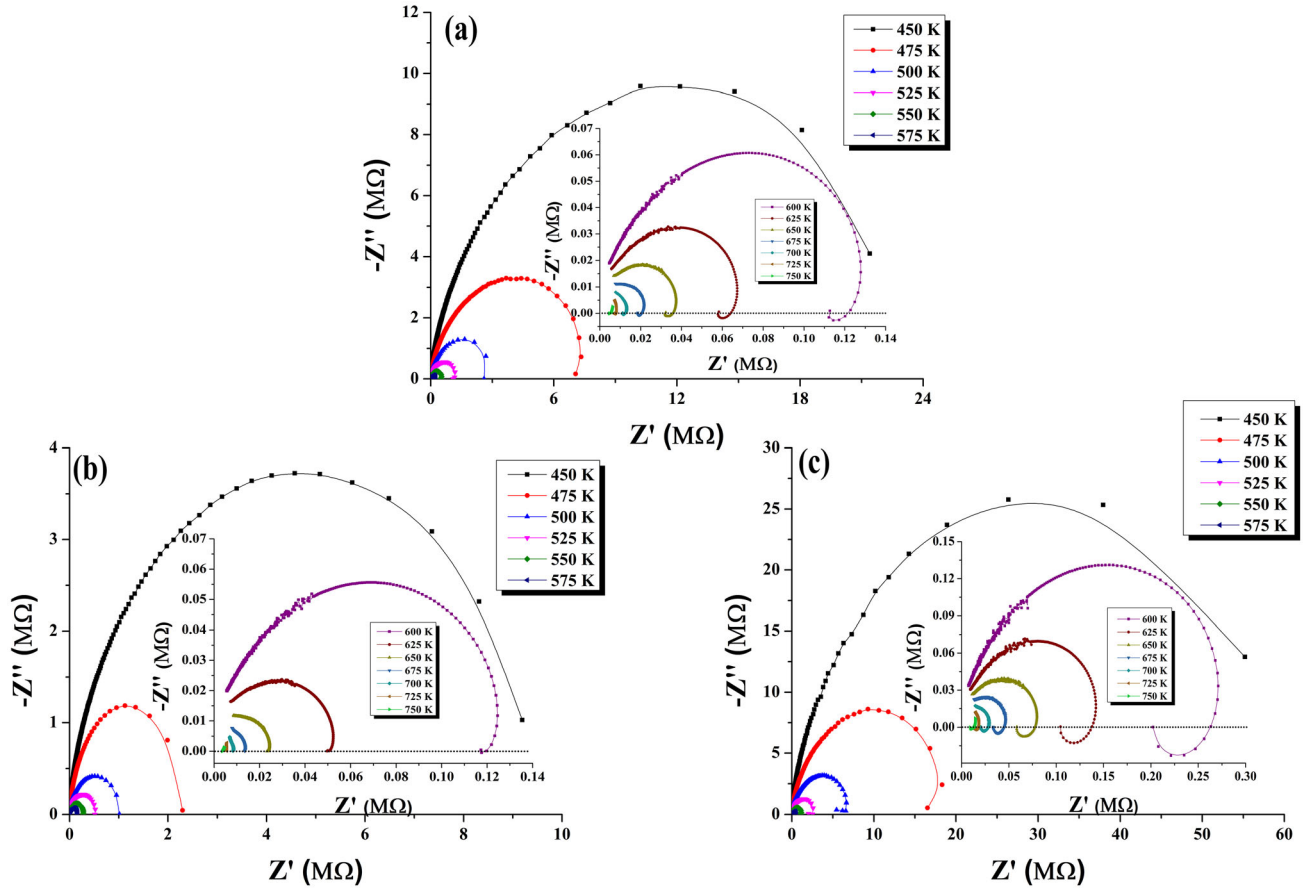


Fig. 5 Z'' versus Z' Nyquist plots at different temperatures for **a** pure ZnO, **b** $Zn_{0.95}Sn_{0.05}O$, and **c** $Zn_{0.90}Sn_{0.10}O$ thin film

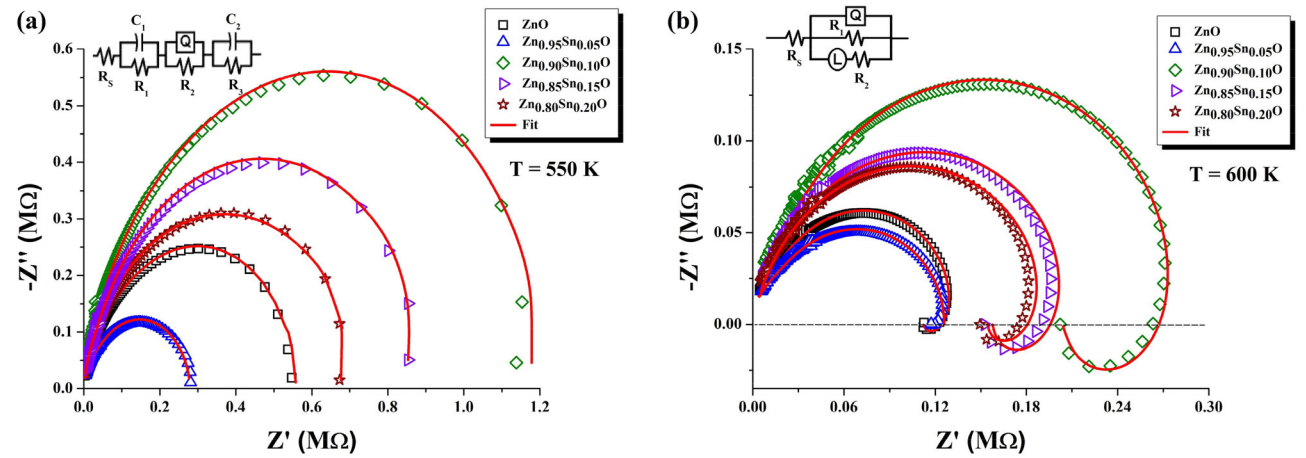


Fig. 6 Equivalent circuit fit of Nyquist plots at **a** T = 550 K and **b** T = 600 K for all the thin films

where Z_{CPE} and Q are, respectively, impedance and capacitance of the CPE. The α values were estimated from the fit analysis for pure ZnO, $Zn_{0.95}Sn_{0.05}O$, $Zn_{0.90}Sn_{0.10}O$, $Zn_{0.85}Sn_{0.15}O$, and $Zn_{0.80}Sn_{0.20}O$ thin films, respectively, as follows: 0.79, 0.87, 0.90, 0.79, and 0.80 at $T = 550$ K and 0.60, 0.56, 0.86, 0.63, and 0.86 at $T = 600$ K. All α values are less than one which suggests that all the films exhibit non-Debye type of dielectric relaxation at both temperatures. However, one critical difference between the two

Table 2 Estimated values of fitting parameters of all the thin films at T = 550 K and T = 600 K

	$T = 550$ K							T = 600 K				
	R_s (MΩ)	R_1 (MΩ)	R_2 (MΩ)	R_3 (MΩ)	C_1 (μF)	C_2 (μF)	Q (μF)	R_s (MΩ)	R_1 (MΩ)	R_2 (MΩ)	L (mH)	Q (μF)
ZnO	0.420	0.022	0.012	0.084	0.661	1.682	2.112	0.116	0.041	0.039	0.095	1.125
$Zn_{0.95}Sn_{0.05}O$	0.222	0.033	0.021	0.077	0.695	1.381	3.267	0.110	0.044	0.043	0.022	1.155
$Zn_{0.90}Sn_{0.10}O$	0.930	0.033	0.017	0.137	0.608	1.770	1.460	0.244	0.070	0.085	0.103	1.084
$Zn_{0.85}Sn_{0.15}O$	0.672	0.025	0.012	0.096	0.619	1.685	1.777	0.177	0.056	0.057	0.098	1.138
$Zn_{0.80}Sn_{0.20}O$	0.526	0.023	0.012	0.087	0.677	1.565	1.584	0.162	0.051	0.049	0.096	1.130

temperatures is the inductance effect that appeared at $T = 600$ K and beyond in the low-frequency region (Fig. 6b).

From Table 2, at $T = 550$ K, it is clear that R_1 and R_2 exhibited almost a constant level of resistances in all the thin films. On the other hand, the 5 wt%-doped ZnO film recorded the lowest resistance R_s and the highest capacitance C_1 with the highest Q value, while the 10 wt%-doped ZnO film showed a complete opposite behavior. This is consistent with $Z'-Z''$ Nyquist plot, where 5 wt.%-doped ZnO film exhibited the smallest semicircle and 10 wt.%-doped ZnO film exhibited the biggest semicircle at $T =$ 550 K (Fig. 6a). In addition to that, at $T = 600$ K, the 5 wt%- and 10 wt%-doped ZnO thin films showed opposite behavior in terms of R_s, L, and Q values, where the former registered lowest R_s, lowest L, and highest Q values, while the latter recorded highest R_s, highest L, and lowest Q values among all other investigated films.

3.3.2 *Modulus study*

Complementary to impedance study, modulus study is another efficient tool to dig deeper into the material and have a clearer view and a more detailed description of the electrical mechanisms therein. The superiority of modulus spectroscopy is the ability to discriminate among different relaxation mechanisms originating in grains, grain boundaries, and grain-electrode interfaces. Contrary to impedance spectroscopy, modulus spectroscopy analyzes the region of smallest capacitance and neglects electrode contributions and, thus, makes it possible to understand separately the effect of each nanostructure on the overall electrical behavior of the film. Moreover, the combination of complex electric modulus, permittivity, and impedance gives the opportunity to investigate long-range conductions and localized dielectric relaxation phenomena in microscopic level [20–22]. The complex electrical modulus can be written in analog to impedance in the form,

$$M^* = M' + iM'', \tag{9}$$

where $M' = C_0\left(\frac{\omega^2 C}{\omega^2 C^2 + G^2}\right)$ and $M'' = C_0\left(\frac{\omega G}{\omega^2 C^2 + G^2}\right)$ are, respectively, the corresponding real and imaginary components of the complex electrical modulus, $\omega = 2\pi f$ is the angular frequency, C is the measured capacitance, G is the measured conductance, $C_0 = \varepsilon_0 \frac{A}{d}$ is the capacitance of free space parallel-plate capacitor, A is the surface area, and d is the thickness of the thin films. Similar to impedance, through modulus analysis, two different types of plots can be analyzed: Bode plots of M' and M'' versus frequency and Nyquist plot of M'' versus M'.

Figure 7 shows the frequency dependence of M' of the films at various temperatures. The low value of M' in the low-frequency region can be a clue to the existence of ionic polarizations in the film structure [23]. Clearly, M' increased as frequency increased and the cutoff frequency at which a change in the behavior is noted shifted to higher frequencies with the increase in temperature. This hints to an increase in dispersion with the increase in temperature and can be attributed to the change in mobility of charge carriers from short range (at low temperatures) to long range (at high temperatures) [23]. In addition to that, all M' plots tend to saturate at high enough frequencies. However, no full saturation was detected at high frequencies which might hint to the presence of electrode polarization effects in the samples [24]. This confirms the presence of CPE in the equivalent circuit of the previous impedance fitting analysis.

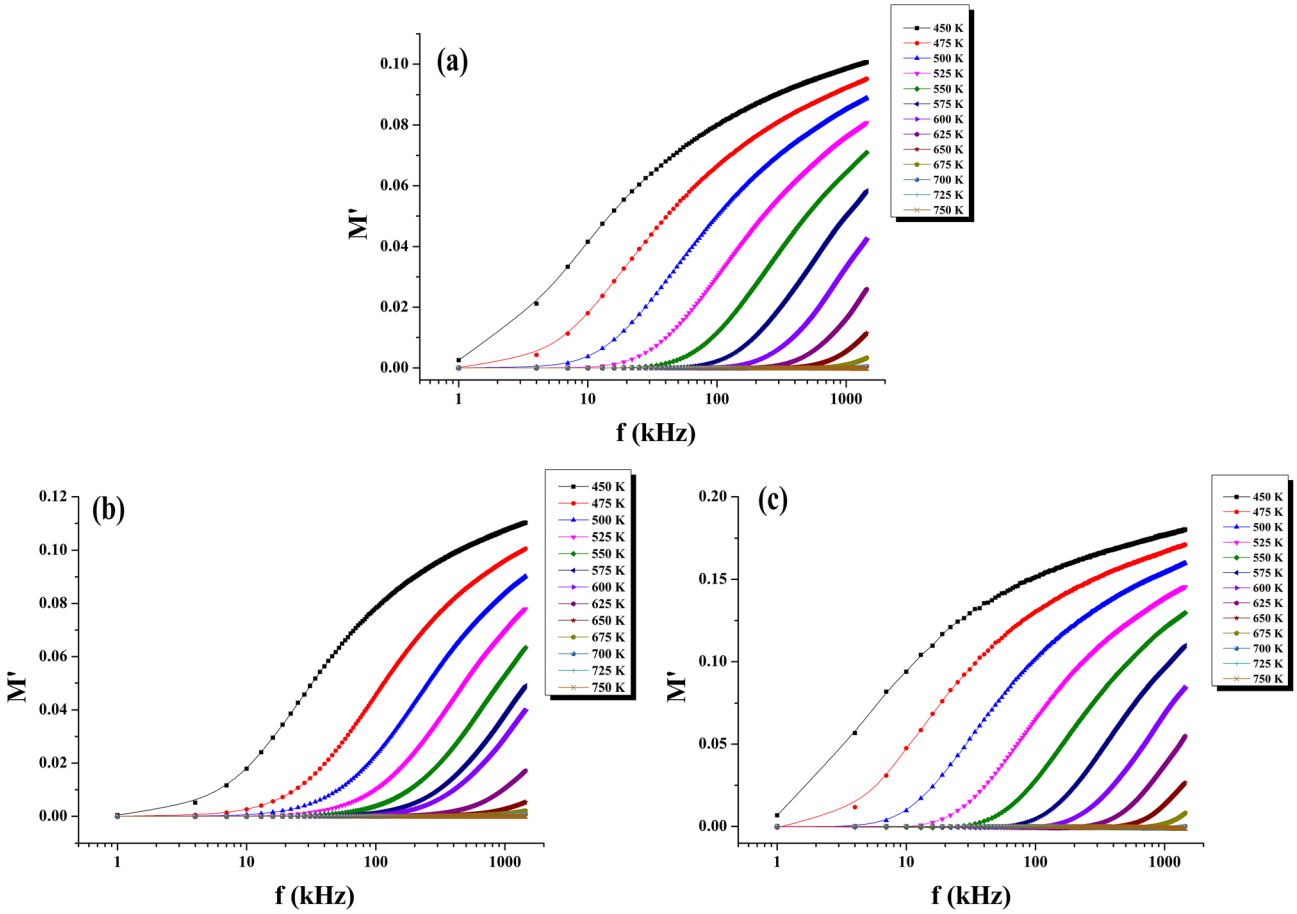


Fig. 7 Frequency response of M' at different temperatures for **a** pure ZnO, **b** $Zn_{0.95}Sn_{0.05}O$, and **c** $Zn_{0.90}Sn_{0.10}O$ thin films

Figure 8 shows the frequency dependence of M'' of the films at various temperatures. M'' is related to energy loss in irreversible conduction processes. Any M'' Bode plot can be regarded as two physically different zones: the low-frequency edge of the peak and the high-frequency edge of the peak. The former represents hopping effects and long-range mobility of charge carriers, while the latter represents confinement effects and short-range mobility of charge carriers [25]. Hence, a peak in Bode plots of M'' represents a dielectric relaxation or a transition from long-range mobility states to short-range mobility states. Clearly, all M'' curves exhibited one relaxation peak that shifted to higher frequencies with temperature increase. Relaxations at low frequencies are usually attributed to effects of interface [16]. And similar to Z'', the shift of peaks to high frequencies hints a decrease in relaxation time at high temperatures, and this signifies that dielectric relaxation processes can be thermally activated. Besides that, independent of temperature, all M'' curves tend to join in the high-frequency region.

Figure 9 shows M'' versus M' Nyquist plots of the films at various temperatures. Generally, such plots can exhibit three different behaviors at three different frequency ranges: semicircular arcs formed at low frequencies correspond to activation of charge carriers in the grain boundary, semicircular arcs formed at high frequencies correspond to activation of charge carriers in the bulk (grain), and entire relaxation semicircles correspond to the total effect of grain, grain boundary, and electrode [22, 26]. In this study, two behaviors were detected as a function of temperature. Up to 575 K, one complete semicircular arc was detected due to the total effect of grains, grain boundaries, and electrodes. This signifies that all nanostructures are well active at relatively low temperatures, and such a semicircular-like response might be an indication of the good electrical properties of the materials. However, at high temperatures (600 K and beyond), all semicircular arcs retracted

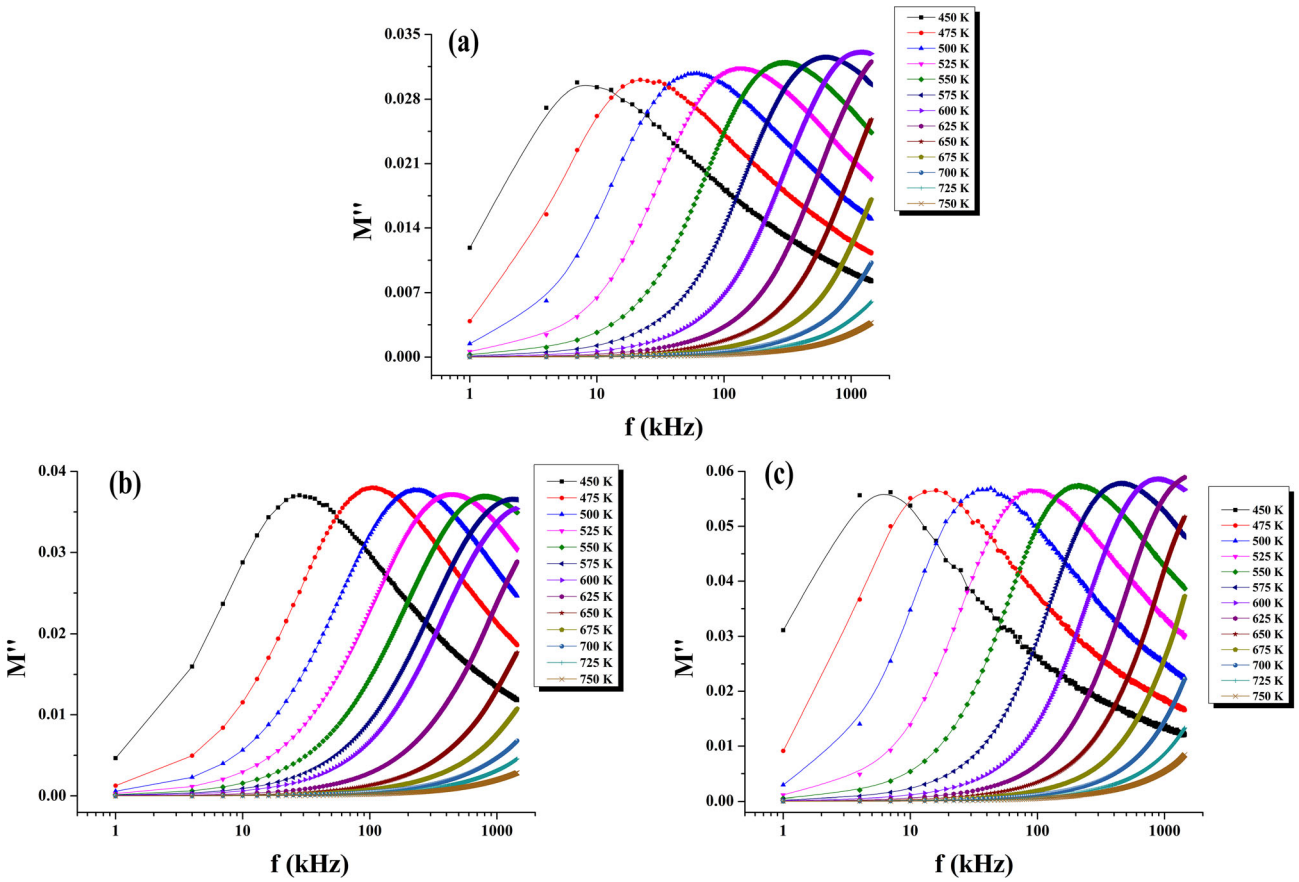


Fig. 8 Frequency response of M'' at different temperatures for **a** pure ZnO, **b** $Zn_{0.95}Sn_{0.05}O$, and **c** $Zn_{0.90}Sn_{0.10}O$ thin films

back and started to appear from the low-frequency side. This behavior signifies that at high temperatures, the low-frequency region and hence grain boundary phase becomes dominant in the film structure. Such outcome can be also seen from the fit analysis (Table 2) where the estimated Q values (representing electrode effects) decreased as the temperature increased from 550 K to 600 K.

The normalized plots of (Z''/Z''_{max}) and (M''/M''_{max}) for the films as a function of frequency at T = 550 K are shown in Fig. 10. Usually, peaks in Z'' and M'' Bode plots are mostly influenced by grain boundary (high resistance region) and grain (low capacitance region), respectively [27]. In ideal Debye relaxations, the two peaks coincide at a specific frequency. Obviously, the two peaks do not coincide in all films. This affirms the outcomes of fitting analysis and confirms that all thin films exhibit non-Debye dielectric relaxation. This reflects the possible occurrence of dipole–dipole interactions in the film structure when exposed to an alternating external electric field.

3.3.3 *DC and AC conductivity studies*

Electrical conductivities of all thin films were measured through (C, G) experimental data set using,

$$\sigma = \left(\frac{\varepsilon_0}{C_0}\right)G, \tag{10}$$

where ε_0 is the permittivity of free space. Figure 11 shows the variation of AC conductivity with frequency of the films at various temperatures. Apparently, all films exhibited similar behavior with different intensities. In general, different conductivity intensities can be associated to many factors like density of oxygen vacancies, quality of crystal structure, and ionic radius of doped atoms [28]. Speaking on the behavior, regarding temperature, conductivity increased as temperature increased. This is a typical semiconductor behavior and it shows that conductivity can be thermally activated and that charge

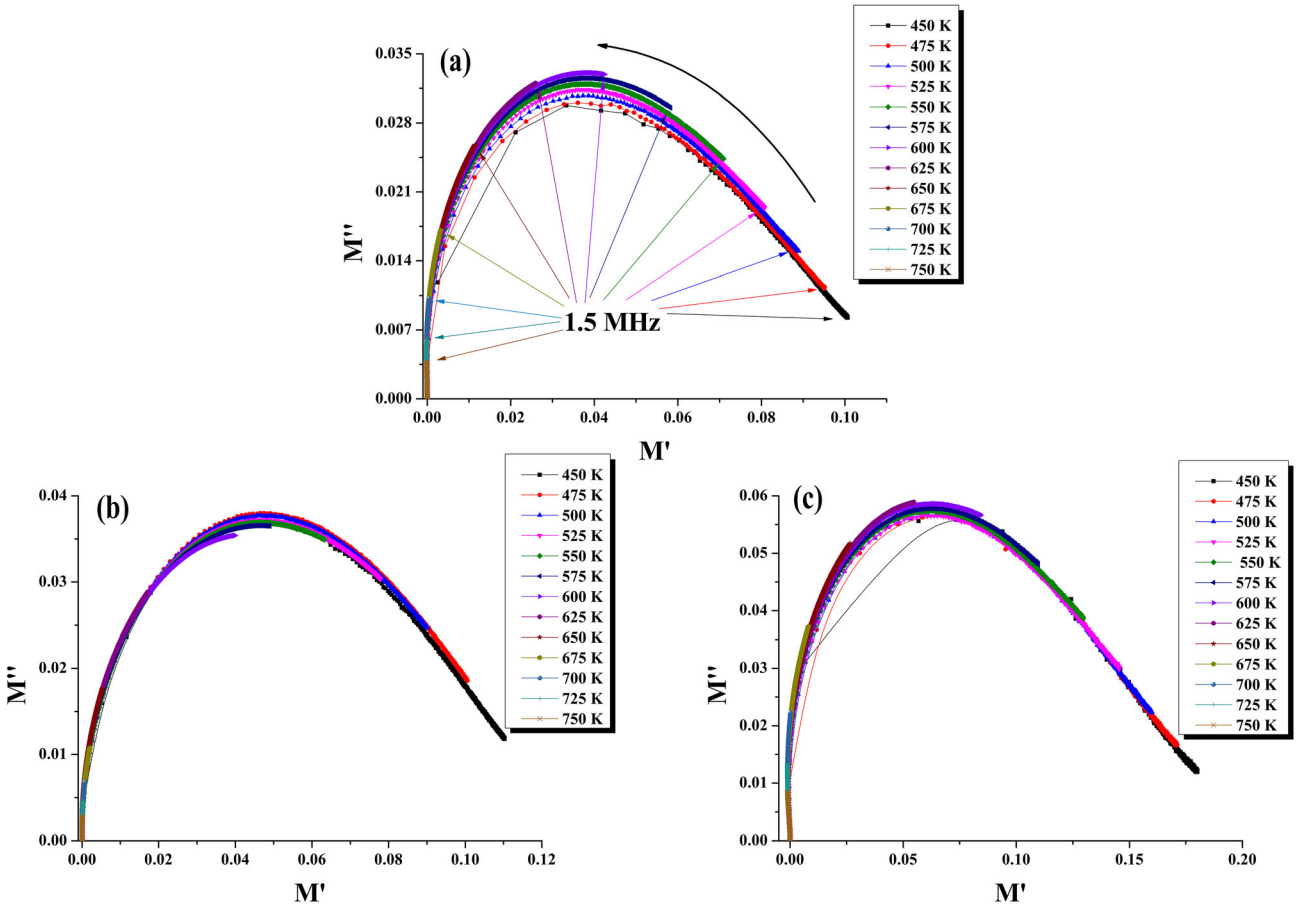


Fig. 9 M'' versus M' Nyquist plots at different temperatures for **a** pure ZnO, **b** $Zn_{0.95}Sn_{0.05}O$, and **c** $Zn_{0.90}Sn_{0.10}O$ thin films

carriers have long-range mobility [19]. Regarding frequency, at low temperatures, as frequency increased conductivity increased. This can be attributed to the hopping mechanism [19] when charge carriers get enough energy to hop from one atomic site to another. It can be also attributed to the decrease in capacitive reactance $X_c = 1/\omega C$ which consequently implies a decrease in the equivalent impedance. On the other hand, at high temperatures, conductivity remained constant and showed an independent behavior of frequency. The alteration of conductivity from AC mode to DC mode at high temperatures can be associated to the fact that charge carriers might have attained their maximum concentration by thermal activation.

From the AC conductivity plots, DC conductivities of all the thin films was extracted from low-frequency region (at $f = 1$ kHz) and were plotted versus temperature as is given in Fig. 12a. In the same manner, Z' of all the thin films was extracted from low-frequency region (at $f = 1$ kHz) and were plotted versus temperature as is given in Fig. 12b. Obviously, as temperature increased from 450 to 750 K, all the thin films showed an increase in σ (or equivalently a decrease in Z') in more than four decades which signifies that conductivity is thermally activated and charge carriers have long-range mobility.

DC conductivity plots and Z' plots obey Arrhenius Eq. [19],

$$f = f_0 \exp\left(-\frac{E_a}{k_B T}\right), \tag{11}$$

where f_0 is a constant known as pre-exponential factor, E_a is the activation energy, k_B is Boltzmann constant, and T is the absolute temperature. Using Eq. (11) and the slope of the best fitting straight lines of $(\ln\sigma)$ and $(\ln Z')$ versus $(1/T)$ given in the insets of Fig. 12, the corresponding activation energies were estimated and tabulated in Table 3. Clearly, the activation energies estimated from the two different data sets match to a great extent. And apparently, 5 wt% and 10 wt% Sn-doped ZnO thin films (exhibiting

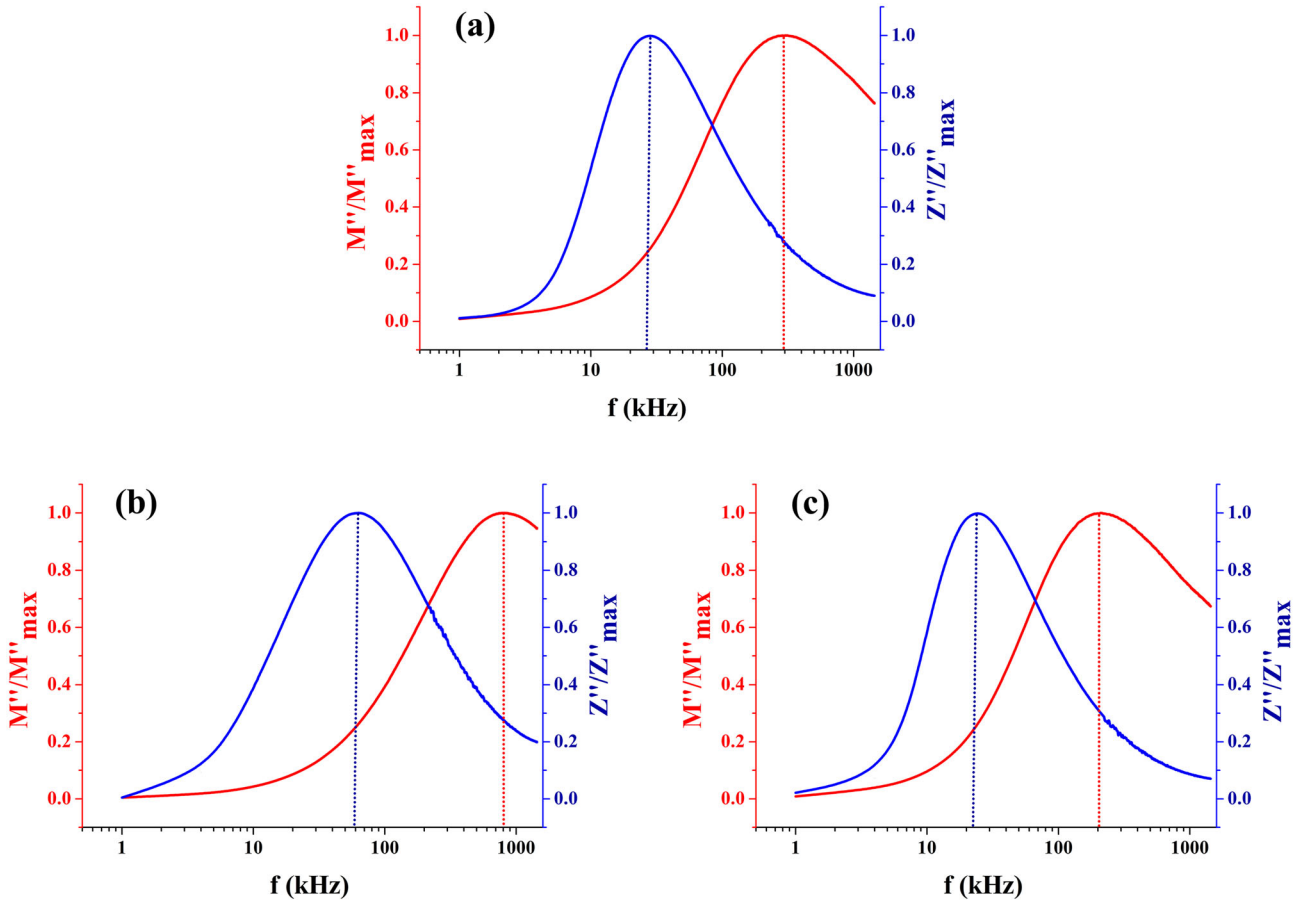


Fig. 10 (Z''/Z''_{max}) and (M''/M''_{max}) versus frequency at T = 550 K for **a** pure ZnO, **b** $Zn_{0.95}Sn_{0.05}O$, and **c** $Zn_{0.90}Sn_{0.10}O$ thin films

respectively the highest and the lowest conductivities) showed, respectively, the lowest and the highest activation energies compared to others.

Ultimately, to clarify the effects of Sn doping on the electrical characteristics of ZnO thin films, the outcomes from impedance, modulus, and conductivity studies at $T = 550$ K, along with the activation energy variation, were superimposed as shown in Fig. 13. Clearly, the electrical characteristics of ZnO thin films changed with Sn doping ratio. 5 wt%-doped films exhibited the highest conductivity, while 10 wt% doped films exhibited the lowest conductivity among all others in the investigated doping range. This was confirmed in terms of the activation energies where 5 wt%-doped films showed the lowest activation energy, while 10 wt%-doped films showed the highest activation energy. Again, this was also confirmed through impedance analysis for which 5 wt%-doped films showed the smallest semicircle (smallest resistance), while 10 wt%-doped films showed the largest semicircle (largest resistance) in impedance Nyquist plots. Besides that, the films with the highest conductivity (5 wt%-doped films) are mainly controlled by grain boundaries due to the shift of the semicircular arc towards low-frequency region in modulus Nyquist plot, while 10 wt%-doped films might be controlled by both grains and grain boundaries.

4 Conclusions

Briefly, in this work, pure ZnO and Sn–doped ZnO (with 5 wt%, 10 wt%, 15 wt%, and 20 wt% Sn) thin films were well synthesized using SILAR method. By XRD technique, structural characterization of the films confirmed the synthesis of hexagonal wurtzite-structured films and suggested a decrease in crystallite size with Sn doping. Moreover, by UV–Vis technique, optical characterization of films proved the good transparency of pure ZnO thin film and showed the increase in transparency and optical

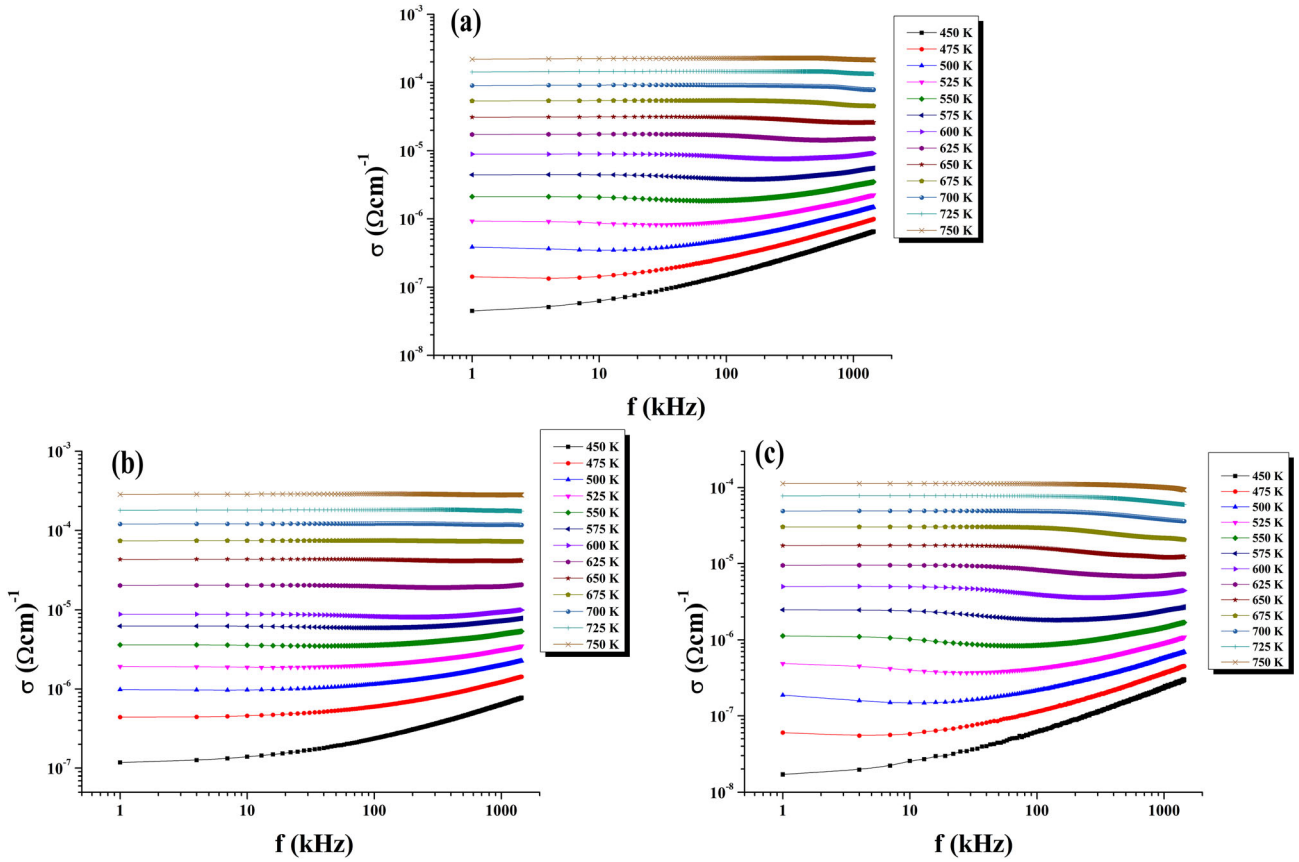


Fig. 11 Frequency response of conductivities at different temperatures for **a** pure ZnO, **b** $Zn_{0.95}Sn_{0.05}O$, and **c** $Zn_{0.90}Sn_{0.10}O$ thin films

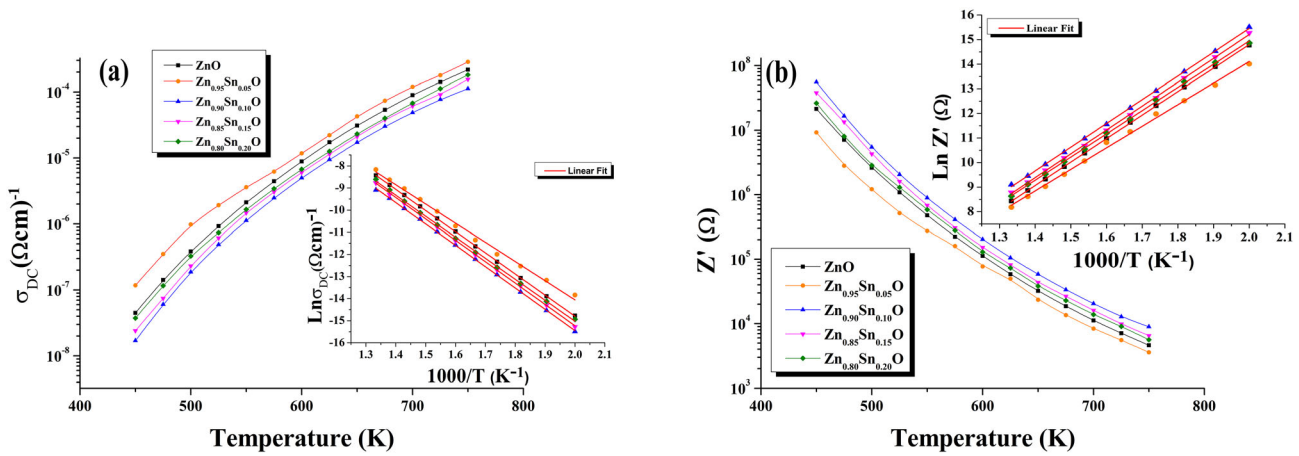


Fig. 12 **a** σ_{DC} versus T and (inset) $ln\sigma_{DC}$ versus $1000/T$, and **b** Z' versus T and (inset) lnZ' versus $1000/T$ at f = 1 kHz for all the thin films

bandgap with Sn doping. Lastly, by impedance, modulus, and conductivity analysis techniques, electrical characterization demonstrated that all the films have a non-Debye type of dielectric relaxation. It also showed that electrode effect is present in all the films at all temperatures, while inductive effect appears only at high temperatures in the low-frequency region. In addition, the analysis demonstrated that 5 wt% Sn-doped ZnO thin film ($Zn_{0.95}Sn_{0.05}O$) exhibits the highest conductivity with the lowest activation energy, and that resistive and capacitive features of the 5 wt%-doped film can be

Table 3 Activation energies estimated from σ and Z' for all the thin films

	E_{a_σ} (eV)	$E_{a_{Z'}}$ (eV)
ZnO	0.82	0.82
$Zn_{0.95}Sn_{0.05}O$	0.75	0.75
$Zn_{0.90}Sn_{0.10}O$	0.93	0.93
$Zn_{0.85}Sn_{0.15}O$	0.89	0.88
$Zn_{0.80}Sn_{0.20}O$	0.82	0.81

mostly referred to the processes that are correlated with grain boundaries only. On the other hand, 10 wt% Sn-doped ZnO thin film ($Zn_{0.90}Sn_{0.10}O$) exhibited the lowest conductivity and the highest activation energy along with the highest possibility of grain domination compared to all other films in the investigated doping range.

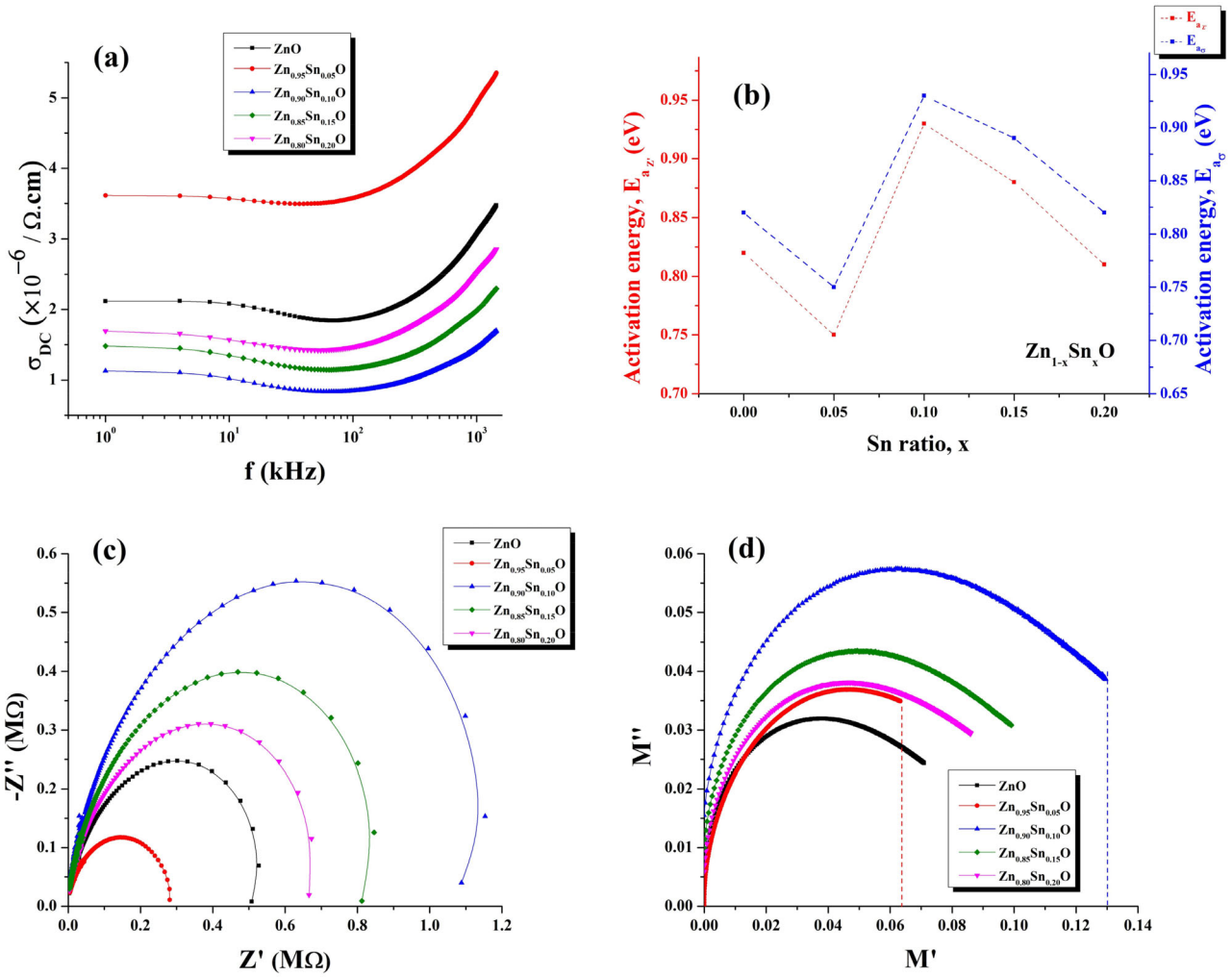


Fig. 13 Superimposition of **a** conductivities, **b** activation energies, **c** impedance Nyquist plots, and **d** modulus Nyquist plots of all the thin films, where a, c, and d correspond to T = 550 K

Acknowledgements

This work was supported by the Scientific and Technological Research Council of Turkey (TÜBİTAK) with Project No. 115M658.

Declarations

Conflict of interest The authors have no conflicts of interest to declare that are relevant to the content of this article.

References

1. Y. Andolsi, F. Chaabouni, M. Abaab, J. Mater. Sci. **28**, 8347–8358 (2017)
2. J.B. Baxter, E.S. Aydil, Sol. En. Mater. Sol. Cells **90**, 607–622 (2006)
3. E. Fortunato, P. Barquinha, A. Pimentel, L. Pereira, G. Gonçalves, R. Martins, Phys. Stat. Sol. **1**, R34 (2007)
4. L. Qiang, X. Liang, Y. Pei, R. Yao, G. Wang, Thin Solid Films **649**, 51–56 (2018)
5. T. Ootsuka, Z. Liu, M. Osamura, Y. Fukuzawa, R. Kuroda, Y. Suzuki, N. Otogawa, T. Mise, S. Wang, Y. Hoshino, Y. Nakayama, H. Tanoue, Y. Makita, Thin Solid Films **476**, 30–34 (2005)
6. S.T. Shishiyanu, T.S. Shishiyanu, O.I. Lupan, Sens. Actuat. B **107**, 379–386 (2005)
7. L. Liu, Z. Mei, A. Tang, A. Azarov, A. Kuznetsov, Q.K. Xue, X. Du, Phys. Rev. B **93**, 235305 (2016)
8. T. Prakash, R. Jayaprakash, C. Espro, G. Neri, E.R. Kumar, J. Mater. Sci. **49**, 1776–1784 (2014)
9. I. Karaduman, A.O. Çağırtekin, T. Çorlu, M.A. Yıldırım, A. Ateş, S. Acar, Bull. Mater. Sci. **10**, 32–42 (2019)
10. F. Zahedi, R.S. Dariani, S.M. Rozati, Bull. Mater. Sci. **37**, 433–439 (2014)
11. V.K. Anand, S.C. Sood, A. Sharma, A.I.P. Conf, Proc. **399**, 1324 (2010)
12. L.H. Kathwate, G. Umadevi, P.M. Kulal, P. Nagaraju, D.P. Dubal, A.K. Nanjundan, V.D. Mote, Sens. Actuat. A **313**, 112193 (2020)
13. N. Nagayasamy, S. Gandhimathination, V. Veerasamy, Open J. Met. **3**, 8–11 (2013)
14. T. Yıldırım, E. Gür, S. Tüzemen, V. Bilgin, S. Köşe, F. Atay, I. Akyüz, Phys. E. **27**, 290–295 (2005)
15. M. Coskun, O. Polat, F.M. Coskun, B. Zengin Kurt, Z. Durmus, M. Caglar, A. Turut, Mater. Sci. Elect. **31**, 1731–1744 (2020)
16. A. Rouahi, A. Kahouli, F. Challali, M.P. Besland, C. Vallee, B. Yangui, S. Salimy, A. Goullet, A. Sylvestre, J. Phys. D **46**, 065308 (2013)
17. L.D. Mosgaard, K.A. Zecchi, T. Heimburg, R. Budvytyte, Membranes **5**, 495–512 (2015)
18. G.J. Brug, A.L.G. Van den Eeden, M. Sluyters-Rehbach, J.H. Sluyters, J. Electroanal. Chem. Inter. Electrochem. **176**, 275–295 (1984)
19. S. Mourad, J. El Ghoul, K. Khirouni, J. Mater. Sci. **31**, 6372–6384 (2020)
20. O. Polat, M. Coskun, F.M. Coskun, J. Zlamal, Z. Durmus, M. Caglar, A. Turut, Mater. Res. Bull. **124**, 110759 (2020)
21. O. Polat, M. Coskun, F.M. Coskun, Z. Durmus, M. Caglar, A. Turut, J. Alloy Compd **752**, 274–288 (2018)
22. S. Karmakar, S. Varma, D. Behera, J. Alloy Compd **757**, 49–59 (2018)
23. M. Azizar-Rahman, A.K.M. Akther-Hossain, Phys. Scr. **89**, 025803 (2014)
24. Ch. Rayssi, S. El Kossi, J. Dhahri, K. Khirouni, RSC Adv. **8**, 17139 (2018)
25. A.K. Pradhan, T.K. Nath, S. Saha, Mater. Res. Exp. **4**, 076107 (2017)
26. P. Choudhary, P. Saxena, A. Yadav, V.N. Rai, A. Mishra, Ionics **25**, 4991–5001 (2019)
27. M. Chandrasekhar, D.K. Khatua, R. Pattanayak, P. Kumar, J. Phys. Chem. Sol. **111**, 160–166 (2017)
28. G.R. Gajula, L.R. Buddiga, K.N. Chidambara Kumar, Res. Phys. **17**, 103076 (2020)

Publisher's Note Springer Nature remains neutral with regard to jurisdictional claims in published maps and institutional affiliations.